

The optimum fire window: applying the fire-productivity hypothesis to Jurassic climate states

Teuntje P. Hollaar^{*1,2}, Claire M. Belcher¹, Micha Ruhl³, Jean-François Deconinck⁴, Stephen P. Hesselbo^{2,5}

¹WildFIRE Lab, Global Systems Institute, University of Exeter, Exeter, EX4 4PS, UK

²Camborne School of Mines, Department of Earth and Environmental Sciences, University of Exeter, Penryn Campus, Penryn, TR10 9FE, UK

³Department of Geology, Trinity College Dublin, The University of Dublin, College Green, Dublin, Ireland

⁴Biogéosciences, UMR 6282 CNRS, Université de Bourgogne/Franche-Comté, 21000 Dijon, France

⁵Environment and Sustainability Institute, University of Exeter, Penryn Campus, Penryn, TR10 9FE, UK

*Corresponding author: t.p.hollaar@uu.nl

Abstract

Present day fire frequency has been related to a productivity/aridity gradient on a regional and global scale. Optimum fire conditions occur at times of intermediate productivity and aridity, whereas fire is limited on the high productivity (moisture) and aridity (no fuel) endmembers. However, the current global fire activity pattern is reinforced by the predominant burning of grasslands. Here we test the intermediate fire-productivity hypothesis for a period on Earth before the evolution of grasses, the Early Jurassic, and explore the fire regime of two contrasting climatic states: the Late Pliensbachian (LPE) cooling Event and the Sinemurian-Pliensbachian Boundary (SPB) warming. Palaeo-fire records are reconstructed from fossil charcoal abundance, and changes in the hydrological cycle are tracked via clay mineralogy, which allows inference of changes in fuel moisture status. Large fluctuations in the fossil charcoal on an eccentricity time scale indicate two modes of fire regime at the time. Wildfires were moisture limited in a high productivity ecosystem during eccentricity minima for both the SPB and LPE. During eccentricity maxima, fires increased, and an optimum fire window was reached, in which greater seasonality in rainfall and temperatures led to intermediate states of productivity and aridity. The LPE experienced more extreme climatic endmembers compared to the SPB, with the fire regime edging closer to ‘moisture limitation’ during eccentricity minima, and more

Deleted: suggested to

Deleted: biased

Deleted: a time period

Deleted:

Deleted:

Deleted: orbital

Deleted: heightened

41 pronounced seasonality during eccentricity maxima, explained by the overall cooler climate at the
42 time. This study illustrates that the intermediate-productivity gradient holds up during two contrasting
43 climatic states in the Jurassic.

44

45 **Plain Language Summary**

46 Fires are limited in year-round wet climates (tropical rainforests, too wet), and in year-round dry
47 climates (deserts, no fuel). This concept, the intermediate-productivity gradient, explains the global
48 pattern of fire activity. Here we test this concept for climate states of the Jurassic (~190 Myr ago). We
49 find that the intermediate-productivity gradient also applies in the Jurassic, despite the very different
50 ecosystem assemblages, with fires most frequent at times of high seasonality.

51

52 **Key Points**

- 53 • The intermediate-fire productivity gradient can be applied to the Jurassic and be utilized to
54 explain [changes in biomass abundance, moisture availability, and fire activity](#).
- 55 • The terrestrial ecosystem surrounding the Cardigan Bay Basin was not year-round dry during
56 the Sinemurian–Pliensbachian Boundary warming Event or the Late Pliensbachian Cooling
57 Event and therefore fire was not aridity limited.
- 58 • Fire activity was strongly influenced by the ~100 kyr and 405 kyr eccentricity cycle during
59 both climatic states, which led to two modes in the fire regime: productivity limited (minima)
60 and the optimum fire-window (maxima).

61

62

63

64

65

66

67

68

69

Deleted: shifts in biomass, rainfall and fire.

71 **1 Introduction**

72 The global distribution of fire at the present day follows the intermediate-productivity hypothesis.
73 This hypothesis suggests that fire activity increases non-linearly along a productivity gradient
74 primarily controlled by biomass and fuel availability (Pausas & Bradstock, 2007; Pausas & Ribeiro,
75 2013). Climate drives fuel availability, structure, and moisture, which are the main determinants of the
76 fire regime. Where the fire regime reflects the frequency, behaviour, type of fire, and the impact on
77 the ecosystem (Bradstock, 2010). Fire is either limited by high moisture in ecosystems with high
78 biomass production, for example in tropical rainforests, or in high aridity and low biomass production
79 ecosystems, with disconnected fuel such as in deserts. This principle explains drought-driven fire
80 regimes and fuel-limited fire regimes (Pausas & Ribeiro, 2013). In humid regions fires are initiated by
81 seasonal aridity which leads to flammable conditions and lower fuel-moisture status. Rising
82 temperatures can lead to increased drought and flammability in high productivity ecosystems and
83 further accelerate this drought-driven increase in fire activity (Pausas & Ribeiro, 2013). In
84 unproductive arid regions it is biomass production that determines fire activity, as the fuel-moisture
85 status would not be limiting (Pausas & Ribeiro, 2013). The optimum window for wildfires is at
86 intermediate productivity levels, such as in the tropical savannahs of today, wherein biomass can
87 accumulate due to seasonal precipitation and fuel becomes available in the dry season when the fuel
88 moisture status decreases (Meyn et al., 2007; Pausas & Bradstock, 2007; Krawchuk & Moritz, 2011;
89 Pausas & Paula, 2012; Pausas & Ribeiro, 2013).

91 The intermediate-productivity concept provides an effective explanation for the distribution of fire on
92 a global and regional scale in the modern day where highest fire activity is found at intermediate
93 moisture availability (Meyn et al., 2007; Krawchuk & Moritz, 2011; Daniu et al., 2012). The
94 observation of high fire activity in ecosystems that are of intermediate aridity and productivity is
95 strongly driven by grass biomes today (Archibald et al., 2018), where >80 % of area burnt is in
96 grasslands (van der Werf et al., 2006). Although the intermediate-productivity gradient hypothesis of
97 the present day is strongly linked to the expanse of grassland habitats, it should not require the
98 presence of grasses to explain the impact of climate and seasonality on fire frequency in other
99 vegetation types. The crucial concept is that an optimum fire window exists when there is a
100 sufficiently moist season that allows fuel growth which is followed by a drier season in which fuel
101 moisture levels are lowered, allowing ignition and fire spread. Since fire has formed an important part
102 of ecosystems and the Earth system since 420 Ma (Glasspool et al., 2004; Glasspool & Gastaldo,
103 2022), we therefore test whether the intermediate-productivity gradient has also existed and if the
104 concept can also be applied in a world before the evolution of grasses.

106 Here we look back at two contrasting climate events in the Early Jurassic, ~190 Myr ago, to assess
107 what evidence there is for the existence of the intermediate-productivity fire gradient at such time

Deleted: concept

Deleted: concept states

Deleted: ingredients

Deleted: of the fires

Deleted: and

Deleted: because

Deleted: lowers

Deleted: However

Deleted: , t

Deleted: .

Deleted: In

Deleted: At the present day,

Deleted: ,

Deleted: thus this vegetation group clearly biases these generalisations (Archibald et al., 2018).

Deleted: is generated

Deleted: ask


Deleted: how long

126 (Fig. 1). The first event, the Sinemurian-Pliensbachian Boundary event (SPB, is marked by global
127 warming, sea-level rise, increased humidity, and a negative carbon-isotope excursion (Ruhl et al.,
128 2016; Haq, 2018; Deconinck et al., 2019; Storm et al., 2020). In contrast, the second event, the late
129 Pliensbachian Event (LPE) is marked by ~5 °C cooling in NW Europe, greater aridity, sea-level fall
130 and a global positive carbon-isotope excursion (e.g. Korte et al., 2015; Ruhl et al., 2016; Haq, 2018;
131 Deconinck et al., 2019; Storm et al., 2020). We couple charcoal, clay and climate data to infer palaeo-
132 fire and the hydrological regimes during both these time intervals.

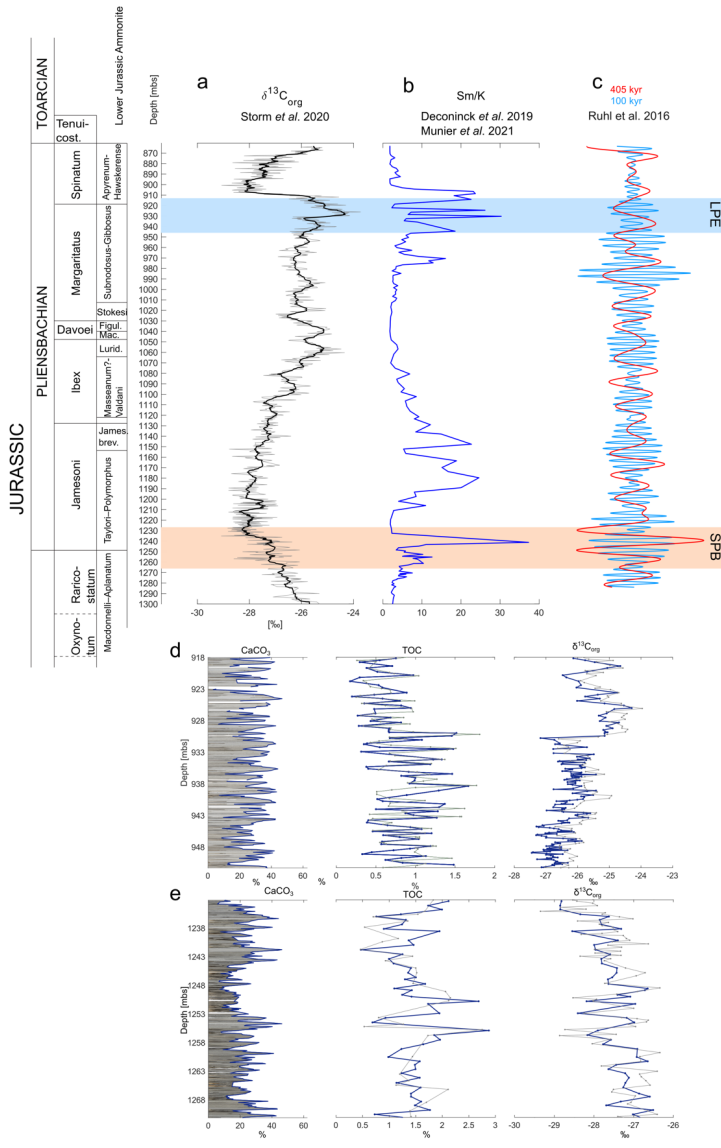
133

134 2 Materials and Methods

135 Materials

136 The records from both time periods  taken from the Llanbedr (Mochras Farm) borehole, from
137 sedimentary strata deposited in a relatively deep marine setting close to the shore in the Cardigan Bay
138 Basin (Wales, UK). These sediments show a strong regular orbital control in the limestone-mudstone
139 alternations (Ruhl et al., 2016), and an existing astrochronological framework provides an age model
140 for the Mochras borehole. In addition, input of terrestrial organic matter in the sampled section is
141 relatively high (van de Schootbrugge et al., 2005; Riding et al., 2013), and thus provides ideal
142 material to study palaeo-fire regimes with a relatively high temporal constraint.

- Deleted:
- Deleted: orbital
- Deleted: scale time
- Deleted:
- Deleted: model
- Deleted: allows for time constraints
- Deleted: input



150

151 **Fig. 1:** Cyclostratigraphic framework of the latest Sinemurian–Pliensbachian of the Mochras core
 152 and the two intervals here studied. Red bar represents the interval (1271–1233 metres below surface
 153 (mbs)) of the SPB and the blue bar represents the interval of the LPE (951–918 mbs) (a) The $\delta^{13}C_{org}$
 154 record from the Mochras core (Storm et al., 2020), shows the broad negative carbon-isotope trend
 155 around the SPB and the positive carbon-isotope excursion (CIE) in the Late Pliensbachian. (b) The

Deleted: <object>

157 smectite/kaolinite (Sm/K) ratio reflects changes in the hydrological cycle; data from Deconinck et al.
158 (2019) and Munier et al. (2021). Peaks in smectite indicate greater climatic aridity (Deconinck et al.,
159 2019; Munier et al., 2021). (c) Bandpass filters of the 100 kyr and 405 kyr cycle based on the Ca-
160 elemental record, in the depth domain from Ruhl et al. (2016). (d) The LPE interval is carbonate-rich
161 and shows the metre-scale variations in CaCO₃ and TOC, next to the δ¹³C_{org} positive shifts that marks
162 the onset of the LPE. (e) The SPB interval contains relatively more clay and lithological couplets of
163 alternating CaCO₃ and TOC-enhanced beds occurring on a metre scale. The δ¹³C_{org} shows the
164 negative trend of the long-negative limb of the SPB negative CIE.

165 The Mochras core was drilled between 1967 and 1969 on the coast in NW Wales, UK. Preserved 1-m-
166 length core slabs of the core are stored at the British Geological Survey National Core Repository at
167 Keyworth, United Kingdom. The Pliensbachian of Mochras shows alternating beds of pale grey
168 limestone and dark brown to grey mudstone (Ruhl et al., 2016). These couplets occur throughout the
169 Pliensbachian, but vary in thickness, from about 90 cm at the Sinemurian–Pliensbachian boundary to
170 about 30 cm in the Late Pliensbachian age strata (latest Margaritatus and Spinatum zones) (Ruhl et al.,
171 2016). The lithological couplets are well expressed around the SPB and in the Margaritatus Zone
172 (Ruhl et al., 2016). For this study, samples were taken at an average sample spacing of 90 cm across
173 the Sinemurian–Pliensbachian boundary (1272–1233 mbs (metres below surface)). In addition, data
174 are utilized in this study that are published in Hollaar et al. (2021; 2023), from the Late Pliensbachian
175 interval that is sampled at a 10 cm (951–934 mbs) and 30 cm (934–918 mbs) resolutions. The
176 macrocharcoal data between 934–918 mbs are new and not previously published. An overview of the
177 number of samples per stratigraphic interval and proxy can be found in SI Table 1.

178 Palaeolocation and provenance

179 During the Early Jurassic, the Mochras site was situated in the Boreal realm of the Laurasian Seaway,
180 which contained an island archipelago, and covers most of present-day NW and W Europe. The
181 Mochras site was situated at a palaeolatitude of ~ 35° N (Torsvik & Cocks, 2017), just off the Welsh
182 Massif, in a relatively deep marine setting, below storm base (Pieńkowski et al., 2021), but with a
183 strong terrestrial influence (van de Schootbrugge et al., 2005; Riding et al., 2013; Xu et al., 2018;
184 Storm et al., 2020).

185 The Welsh Massif was likely the main detrital source to the Cardigan Bay Basin (Deconinck et al.,
186 2019), although other emergent areas in proximity likely also contributed (Deconinck et al., 2019).
187 The nearby Irish Massif, situated west of the Welsh Massif, also cannot be dismissed as a source of
188 nutrients, terrestrial organic particles, clay and coarser mineral grains, to the Cardigan Bay Basin
189 (Deconinck et al., 2019). Another possible source area is the emergent land of the Scottish Massif to
190 the north of the Mochras Borehole and the London-Brabant Massif to the east of the Mochras
191 Borehole (van de Schootbrugge et al., 2005).

Deleted: Orbital

Deleted: and Ti

Deleted: s

Deleted: tion

Formatted: Font: (Default) Times New Roman, 11 pt

Formatted: Font: (Default) Times New Roman, 11 pt, Not Italic

Formatted: Font: (Default) Times New Roman, 11 pt

Deleted: however

Formatted: Font: (Default) Times New Roman, 11 pt

Deleted: can

Formatted: Font: (Default) Times New Roman, 11 pt

Deleted: s

Deleted: could be

Formatted: Font: (Default) Times New Roman, 11 pt, Not Italic

Formatted: Font: (Default) Times New Roman, 11 pt

Formatted: Font: (Default) Times New Roman, 11 pt

Formatted: Font: (Default) Times New Roman, 11 pt

Deleted: south

Formatted: Font: (Default) Times New Roman, 11 pt

Formatted: Font: (Default) Times New Roman, 11 pt

Formatted: Font: (Default) Times New Roman, 11 pt, Not Italic

Formatted: Font: (Default) Times New Roman, 11 pt

201 The multiple nearby landmasses contributing runoff to the here studied relatively deeper marine
202 depositional environment, allowed for the charcoal record presented in this study to reflect a regional
203 expression of likely multiple fires. It is important to note, that one stratigraphic rock sample in this
204 study represents a ~2 kyr average signal, which likely is more than the fire return interval at the time
205 of deposition. And thus represents an averaging of the overall fire signal. Therefore, the term ‘fire
206 activity’ here describes the overall occurrences as increases and decreases in wildfires across the
207 region.

Deleted: mari

Deleted: seaway,with

Deleted: ,

208 *Methods*

209 Mass spectrometry $\delta^{13}\text{C}_{\text{org}}$, TOC and CaCO_3

210 Bulk organic carbon-isotopes, TOC and carbonate content were measured to track changes in the
211 carbon-cycle and changes in total organic matter in the studied interval. For the SPB interval (1271–
212 1233 mbs) 50 samples and for the LPE (918–951 mbs) 193 samples were processed for carbon
213 isotope mass spectrometry. Bulk rock samples were powdered using a pestle-a-mortar, weighed into
214 centrifuge tubes, and decarbonated using 3.3 % HCl. Following, the samples were transferred to a hot
215 bath (79 °C) for 1 h to remove siderite and dolomite. After this, the samples were centrifuged and the
216 liquid decanted, this step repeated until the samples were neutralized (on average 2 times). Finally, the
217 samples were oven-dried, re-powdered, and weighed (to measure CaCO_3 loss) and transferred into
218 small tin capsules for mass spectrometry (TOC and $\delta^{13}\text{C}_{\text{org}}$), at the University of Exeter, Penryn
219 Campus.

Deleted: 934

Deleted: 918

Deleted: 43

220 Charcoal quantification and palynofacies

221 For the SPB interval, 54 samples were prepared for charcoal analysis and 42 for palynofacies at the
222 University of Exeter, Streatham Campus. For the LPE interval, an additional 50 macrocharcoal
223 samples were analysed, to compliment a total of 204 macrocharcoal samples for this interval. A total
224 of 162 samples for palynofacies and 200 microcharcoal samples are included in the LPE study
225 interval.

226 Rock samples of 10–30 g weight were split into 0.5 cm³ fragments to minimize the breakage of the
227 organic particles whilst optimizing the surface area for palynological acid maceration. First, the 190
228 samples were treated with 10 % and 37 % HCl to remove carbonate. After this, hydrofluoric acid (40
229 % HF) was added to remove silicates from the sample. The samples were left to digest for 48 h, after
230 which cold concentrated HCl (37 %) was added to avoid calcium fluoride precipitation. Each sample
231 was left to settle, after which it could be decanted and topped up with DI water, a step that was
232 repeated ~ 6 times in order for the sample to neutralize.

233 After neutralizing, 5 droplets of the mixed residue were taken for the analysis of palynofacies (total
234 particulate organic matter) prior to any sieving. The remaining residue was sieved through a 125 µm
235 sieve and a 10 µm sieve to retrieve the macroscopic fraction (> 125 µm) and microscopic fraction

242 (10–125 µm). Macroscopic charcoal (>125 µm) was quantified using a Zeiss Stemi microscope, with
243 a 10 x 4 magnification lens and top lighting from a ‘goose necked’ light source. The entire
244 macroscopic fraction was dispersed in a Petri dish filled with DI water and the number of charcoal
245 particles counted and expressed per 10 g of processed rock (n/g). In some samples large clusters of
246 matrix were not digested by the acid, in which case they were taken out and dry weighed to deduce
247 the weight of the total processed rock. Charcoal particles are identified as opaque, black, angular,
248 reflective of light, with lustrous shine, elongated, lacking brown edges, and splintering during
249 breakage, and often showing the anatomical structure of the plant preserved (SI Fig. 1 and SI Table 2,
250 Scott, 2000; Scott & Damblon, 2010).

Deleted: and

Deleted: no brown edges,

251 Microscopic charcoal (10–125 µm) was analysed on a palynological slide. A known quantity of 125
252 µl of the microscopic fraction was mounted onto microscopic slides using glycerine jelly. A
253 transmitted light microscope (Olympus (BX53)) with a 40 x 10 magnification was used to count the
254 charcoal particles. Four transects per slide were counted, one transect on the left, two in the middle,
255 and one on the right of the coverslip. These data were then scaled up to the known quantity of the total
256 sample (Belcher et al., 2005). Palynofacies were examined to record shifts in the type of organic
257 matter (terrestrial vs marine) and potential changes in organic matter preservation and/or terrestrial
258 runoff. Palynofacies were quantified using the optical light microscope and a minimum of 300 organic
259 particles per palynological slide was counted. The types of organic matter were roughly grouped after
260 Oboh-Ikuenobe et al. (2005): terrestrial palynomorphs (spores and pollen), marine palynomorphs
261 (dinoflagellates, acritarchs, prasinophytes and foraminifera test linings), fungal remains, structured
262 phytoclasts (wood particles, parenchyma), unstructured phytoclasts (degraded plant remains),
263 charcoal, black debris (palynomorphs filled with pyrite) and amorphous organic matter (AOM: fluffy,
264 clotted and granular masses, colour ranging between almost colourless to yellow and pale brown).

265 XRD clay mineralogy

266 A total of 55 samples were prepared for clay mineralogy spanning the SPB interval and 194 samples
267 for the LPE interval. About 5 g of bulk-rock sample was gently crushed and powdered with an agate
268 mortar, after which about 2–3 g of the powdered sample was decarbonated with a 0.2 M HCl solution.
269 The samples were left to settle for 95 min, after which the suspended clay sized fraction (< 2 µm) was
270 extracted with a syringe (following Stokes’ law). The clay fraction was centrifuged and subsequently
271 smeared and oriented on glass slides. The samples were analysed by X-ray diffraction (XRD) using a
272 Bruker D4 Endeavour diffractometer (Bruker, Billerica, MA, USA) with Cu K α radiations, LynxEye
273 detector and Ni filter under 40 kV voltage and 25 mA intensity at the Biogéosciences Laboratory,
274 Université Bourgogne/FrancheComté, Dijon. Three runs were performed per sample to discriminate
275 the clay phases: (1) air-drying at room temperature; (2) ethylene-glycol solvation for 24 h; (3) heating
276 at 490 °C for 2 h, following Moore & Reynolds (1997). Comparing the three diffractograms obtained,
277 the clay minerals were identified using their main diffraction (d0001) peak. The proportions of each

280 clay mineral on glycolated diffractograms was estimated with the MACDIFF 4.2.5 software
281 (Petschick, 2000). The identification of the clay minerals further follows the methods in Moore &
282 Reynolds (1997) and Deconinck et al. (2019).

283 Statistical analysis

284 Orbital filters and the charcoal record

285 The Pliensbachian of the Mochras core has a well-established astrochronological framework (Ruhl et
286 al., 2016; Hinnov et al., 2018; Storm et al., 2020; Hollaar et al., 2021; Pienkowski et al., 2021). Based
287 on the existing cyclostratigraphy, the 100 kyr eccentricity cycle lies within the range of 3.2–10.2 m
288 (Ruhl et al., 2016; Hinnov et al., 2018), 6.3–4.8 m (Storm et al., 2020), and ~5.3 m (Pieńkowski et al.,
289 2021) for the [here](#) studied SPB and LPE intervals. ~~These intervals each compromise ~7–8 short~~
290 eccentricity cycles. No spectral analysis has been performed on the records presented here because of
291 the limited time span represented. Instead, we compare the charcoal and clay records visually with the
292 100 kyr and 405 kyr filters based on Ca and Ti (Ruhl et al., 2016; Hinnov et al., 2018). [In SI Fig. 2 we](#)
293 [overlay the 3.2 – 10 m filter \(based on Ruhl et al., 2016\) derived from the macrocharcoal record with](#)
294 [the normalized dataset of the macrocharcoal record.](#)

295 Pearson correlation

296 A Pearson correlation was used to test for possible correlation between the charcoal abundance (both
297 size fractions) and palynofacies and the significance using RMatlab2021. The p value tests the
298 hypothesis of no correlation against the alternative hypothesize of a positive or negative correlation,
299 with the significance level at p = 0.05. See SI Fig. 3.

300 Wilcoxon test

301 A Wilcoxon rank sum test was performed in RMatlab2023b to test the H0 hypothesis of equal means
302 between the charcoal populations of the LPE and the SPB interval with the significance level at p =
303 0.05. The test is performed for the macrocharcoal and microcharcoal records separately.

304 PCA analysis

305 Principal component analysis (PCA) was performed to explore the potential correlation of charcoal,
306 clay mineralogy, palynofacies and mass-spectrometry records for the two studied intervals. This was
307 executed in the software PAST on the normalized dataset (macrocharcoal, microcharcoal, TOC,
308 CaCO₃, δ¹³C_{org}, S/I, Sm/K, K/I, phytoclasts).

309 **3 Results**

310 The data presented here that cover the run-up to and onset of the SPB (1271–1233 mbs) show a ~1.8
311 ‰ negative shift in δ¹³C_{org} spanning the end of the negative CIE limb in the Mochras borehole and
312 reaching most negative values. The results of the LPE interval which encompass the run-up and onset
313 of the LPE (951 – 918 mbs), show a rapid positive shift in the δ¹³C_{org} of ~1.8 ‰ (between 930.8 –

Deleted: here

Deleted: studied intervals of the SPB and LPE

Deleted: 8

Deleted: 9

Formatted: Underline

Formatted: Font: (Default) Times New Roman, 11 pt, Font colour: Auto, Pattern: Clear

Formatted: Font: (Default) Times New Roman, 11 pt, Font colour: Auto, Pattern: Clear

Formatted: Font: (Default) Times New Roman, 11 pt, Font colour: Auto, Pattern: Clear

Formatted: Font: (Default) Times New Roman, 11 pt, Font colour: Auto, Pattern: Clear

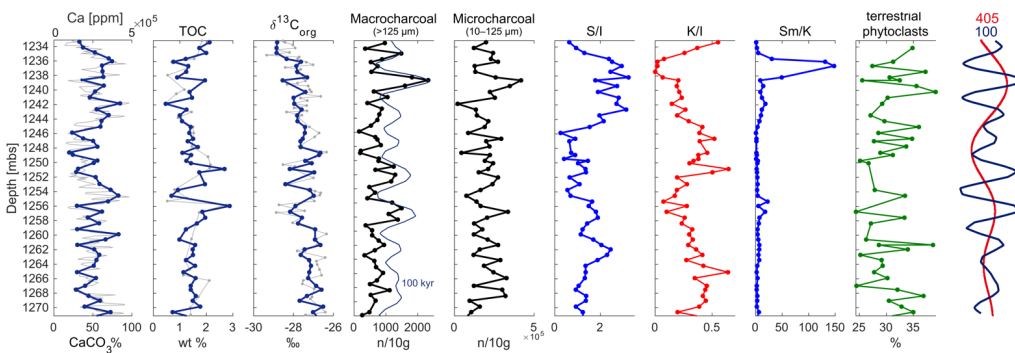
Formatted: Font: (Default) Times New Roman, 11 pt, Font colour: Auto, Pattern: Clear

Formatted: Subscript

Formatted: Superscript

Formatted: Subscript

318 930.4 mbs) (in agreement with Storm et al., 2020).
 319 Large fluctuations are observed in the abundance of both macroscopic (>125 µm) and microscopic
 320 (10–125 µm) fossil charcoal for both CIEs. For the SPB, microcharcoal abundance fluctuates from
 321 2×10^4 – 4.2×10^5 (mean 2×10^5) particles per 10 g of sediment, and the number of macrocharcoal
 322 particles varies from 99–2327 (mean 787) particles per 10 g sediment (Fig. 2, SI Table 3). A similar
 323 trend is observed in both size fractions, with individual charcoal peaks fluctuating on a 2–4 m scale
 324 (Fig. 2). In the higher resolution LPE interval, metre-scale individual peaks of charcoal abundance are
 325 observed, with microcharcoal abundance fluctuating from 4.5×10^3 – 4.3×10^5 (mean 1.1×10^5) particles
 326 per 10 g of sediment, and the number of macrocharcoal particles varies from 8–2276 (mean 376)
 327 particles per 10 g sediment (Fig. 3, SI Table 3). Longer term fluctuations in the macrocharcoal record
 328 are also observed, with bundling of peaks visible every ~4–5 m. Micro- and macro-charcoal are more
 329 abundant in the SPB compared to the LPE (Fig. 4). The outcome of the Wilcoxon signed rank test
 330 confirms a different median of the SPB and LPE macrocharcoal (H0 rejected, p<0.001) and
 331 microcharcoal (H0 rejected, p<0.001).



332 **Fig. 2: The SPB studied interval showing all proxies of this study in context of the orbital filters**
 333 **(Ruhl et al., 2016).** The CaCO_3 , TOC and $\delta^{13}\text{C}_{\text{org}}$ (blue) data obtained for the present study are
 334 plotted over previously published data (light grey – Ruhl et al., 2016; Storm et al., 2020). The
 335 macrocharcoal abundance shows ~8 increases and decreases throughout the studied interval. These
 336 high-low intervals in the macrocharcoal record correspond to the 100 kyr filter (blue; and see SI Fig.
 337 2). The majority of macrocharcoal peaks are mirrored in the microcharcoal fraction. Alternating
 338 phases of increase in the smectite/illite ratio (S/I) and the kaolinite/illite ratio (K/I) indicate swings in
 339 the hydrological cycle. This is further indicated by the smectite/kaolinite ratio (Sm/K). The percentage
 340 of terrestrial phytoclasts shows that the terrestrially sourced organic particles fluctuate around 30%
 341 in the studied interval. Finally, the bandpass filters of Ruhl et al. (2016) based on the Ca-elemental
 342

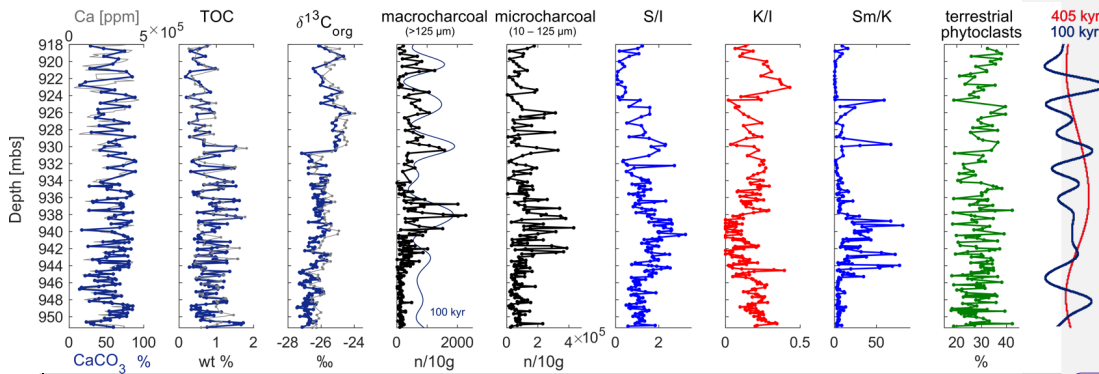
Deleted: <object>

Deleted: 5

Deleted: peaks

Deleted: orbital

347 **XRF** record indicate that the clay records shift dominance on a 405 kyr time scale. The peaks in the
 348 macrocharcoal record occur on a 100 kyr time scale (see also SI Fig. 2).



349 **Deleted: <object>**

350 **Fig. 3: Synthesis of the LPE interval showing all proxies considered in this study in context of the**
 351 **orbital filters (Ruhl et al., 2016).** The CaCO_3 , TOC and $\delta^{13}\text{C}_{\text{org}}$ (blue) from Hollaar et al. (2023) are
 352 plotted over independently generated data (light grey - Ruhl et al., 2016; Storm et al., 2020). The
 353 macrocharcoal abundance shows ~7 peaks throughout the studied interval. *These 7 increases and*
 354 *decreases in macrocharcoal abundance correspond to the 100 kyr eccentricity (in blue, see SI Fig. 2).*
 355 The majority of macrocharcoal peaks are mirrored in the microcharcoal fraction. Alternating phases
 356 of increase in the smectite/illite ratio (S/I) and the kaolinite/illite ratio (K/I) indicate swings in the
 357 hydrological cycle. This is further indicated by the smectite/kaolinite ratio (Sm/K). The percentage of
 358 terrestrial phytoclasts shows that the terrestrially sourced organic particles fluctuate around 30 % in
 359 the studied interval. Finally, the orbital filters of Ruhl et al. (2016) are placed next to the proxy
 360 records. This shows that the clay records shift dominance on a 405 kyr time scale. The peaks in the
 361 macrocharcoal record occur on a 100 kyr time scale.

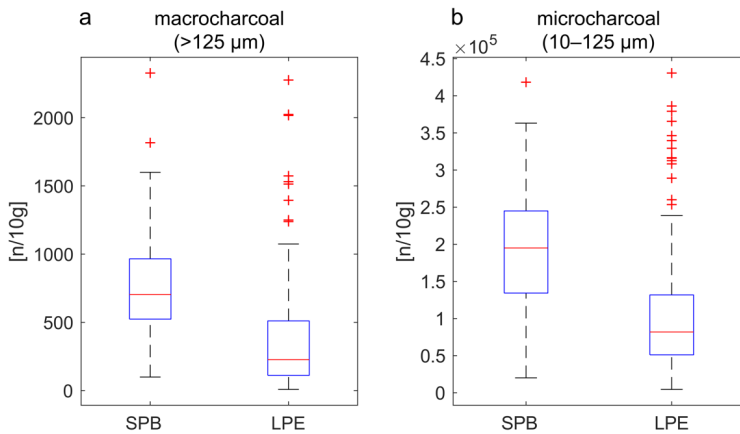
362

363 The palynofacies of both intervals is typically marine (AOM>58%). The proportion of terrestrial vs
 364 marine organic matter remains relatively stable through both the SPB and LPE, varying between 24.4
 365 and 39.1% (mean 30.7%), and 17.7 and 42.3% (mean 28.9%), respectively. Charcoal accounts for
 366 ~3.7% and ~4.5% of the total particulate organic matter, respectively for the SPB and the LPE
 367 intervals (SI Fig. 4). The abundance of macrocharcoal is not influenced by the percentage of terrestrial
 368 particulate organic matter through the SPB and LPE intervals (SPB $r = -0.12$, $p = 0.42$; LPE $r = 0.06$,
 369 $p = 0.46$) and nor is the microcharcoal abundance for the SPB interval ($r = 0.07$, $p = 0.62$). However, a
 370 very weak correlation exists between the percentage of terrestrial phytoclasts and microcharcoal
 371 abundance in the LPE interval ($r = 0.16$, $p = 0.05$). These results suggest that the preservation and/or

Deleted: 5

Deleted: 1

375 influx of terrestrial particulate organic matter is not the main driver of fluctuations in charcoal
 376 abundance.



377
 378 **Fig. 4:** Distribution boxplots of the macrocharcoal and microcharcoal abundance of the SPB and
 379 LPE studied intervals. (a) Average macrocharcoal abundance is higher in the SPB interval compared
 380 to the LPE interval, however, the absolute minimum and maximum are similar. (b) Average
 381 microcharcoal abundance is higher for the SPB compared to the LPE. The minimum number of
 382 microcharcoal particles is lower for the LPE, however, the maximum microcharcoal abundance is
 383 similar in both records.

384
 385 The clay mineral assemblages of the SPB and LPE are dominated by illite, kaolinite and smectite (I-S
 386 R0), with smectite increasing in parallel with decreases of illite and kaolinite (SI Fig. 5). Low
 387 proportions of chlorite and sparse I-S R1 are present in the SPB record. Chlorite and I-S R1 are
 388 generally low in the LPE record but increase between 924–219 mbs (SI Fig. 5). Two smectite-
 389 enhanced phases occur for the SPB, at 1264–1255 mbs and 1245–1235 mbs. Both these phases are
 390 coeval with high charcoal abundance (both size fractions) (Fig. 2, SI Fig. 6). Additionally, the LPE
 391 interval encompasses two stratigraphic intervals rich in smectite; from 944–937 mbs and 931–924
 392 mbs. Charcoal abundance (both size fractions) increases overall, and coevally with the S/I, over ~ 5 m
 393 scale fluctuations, and decreases at levels with high K/I (Fig. 3, SI Fig. 7). The 3.2–10.2 m orbital
 394 filter of the macrocharcoal records (interpreted as the 100 kyr eccentricity (Ruhl et al., 2016; Hinnov
 395 et al., 2018; Storm et al., 2020; Pienkowski et al., 2021)), indicates that the observed fluctuations in
 396 the macrocharcoal record occur with a 100 kyr periodicity (SI Fig. 2).

397

Deleted: <object>

Deleted: 2

Deleted: 2

Deleted: 6

402 **4 Discussion**

403 *Charcoal transport and preservation*

404 The charcoal records for both the SPB and LPE intervals do not appear to be linked to the terrestrial
405 influx of materials, as evidenced by the palynofacies. No parallel trends are observed between the
406 abundance of terrestrial phytoclasts and the number of charcoal particles, which suggests that the
407 abundance of charcoal is not a reflection of preservation and/or runoff changes. Inferred sea level
408 changes during the LPE and the SPB could potentially have impacted the charcoal abundance record
409 and the clay mineralogy. Transgression and relative sea-level rise during the SPB has been extensively
410 recorded from the Boreal and Tethys regions, and from South America (e.g. Legarreta and Uliana,
411 1996; de Graciansky et al., 1998; Hesselbo & Jenkyns, 1998; Danisch et al., 2019; Silva et al., 2021).
412 The Late Pliensbachian is characterized by widespread regressive facies and inferred relative sea-level
413 fall, likely indicating a closer proximity to shore also in the Mochras borehole. Fossil wood in the
414 Mochras borehole has been shown to become more abundant at this time, suggesting a potential bias
415 of higher terrestrial input from a nearby landmass (Ullmann et al., 2022). However, the mean
416 abundance of macrocharcoal and microcharcoal is higher during the SPB (mean of 787 and 2×10^5
417 respectively) compared to the LPE (mean of 376 and 1.1×10^5 respectively) in the Mochras borehole,
418 suggesting that the shore proximity did not impact overall charcoal abundance. Similarly, the
419 palynofacies analysis indicates that the mean abundance of terrestrial particulate organic matter during
420 the SPB (30.7%) is not higher compared to the LPE (28.9%). Hence, we take this as strong evidence
421 that the record of fossil charcoal records changes in wildfire activity.

422 *Orbital forcing of the hydrological cycle and fire*

423 Alternations in the dominance of smectite and kaolinite occur approximately every 10 m in both the
424 LPE and SPB records. Kaolinite and smectite reflect hydrological changes in the palaeoenvironment
425 of the Cardigan Bay Basin (Deconinck et al., 2019; Munier et al., 2021). As the smectite and kaolinite
426 clay minerals are detrital in character and their abundance varies in opposition to one another (Fig. 2
427 and 3), these clays are likely derived from pedogenic weathering profiles (Deconinck et al., 2019).
428 Smectite preferentially forms under a hot and seasonally arid climate, similar to a monsoonal climate
429 system or the winter-wet climate of the Mediterranean zone (Chamley, 1989; Deconinck et al., 2019).
430 Kaolinite is indicative of an accelerated hydrological cycle, increased runoff and a year-round wet
431 climate (Chamley, 1989; Ruffell et al., 2002) either via formation in strong weathering profiles or via
432 the physical erosion of kaolinite-bearing rocks (Chamley, 1989). At times of high smectite abundance,
433 fire activity is greatest as observed from the macro- and micro-scopic charcoal fractions (Fig. 2 and
434 3). Based on the astrochronological framework of the Mochras borehole (Ruhl et al., 2016; Hinnov et
435 al., 2018; Storm et al., 2020; Pieńkowski et al., 2021) these alternations appear to occur in concert
436 with the 405 kyr long-eccentricity cycles (Fig. 2, Fig. 3). Eccentricity modulates the precession driven
437 changes in seasonal and latitudinal distribution of insolation (Imbrie & Imbrie, 1980; Berger et al.,

438 1989). One ~20 kyr precession cycle can represent a strongly seasonal extreme climate for ~10 kyr
439 and a weakly seasonal climate for the subsequent ~10 kyr. The geological record averages the
440 amplification or suppression of seasonality between years (SI Fig. 8). Eccentricity forcing modulates
441 the amplitudes of these extremes in seasonality with periodicities of 100 kyr and 405 kyr.

Deleted: 4

442 In the Mesozoic, eccentricity maxima are commonly associated with dry climates that are disrupted
443 by short and intense periods of precipitation and storm activity in the boreal landmasses bordering the
444 NW Tethys (Martinez & Dera, 2015). In contrast, eccentricity minima are characterized by a more
445 moderate seasonal contrasts and year-round wet conditions (Martinez & Dera, 2015). Eccentricity
446 minima are linked to periods of enhanced runoff and weathering conditions as evidenced by high
447 kaolinite content, $^{87}\text{Sr}/^{86}\text{Sr}$, and negative shifts in $\delta^{18}\text{O}$ (Martinez & Dera, 2015). Therefore, we link
448 the observed smectite-rich intervals to eccentricity maxima and the kaolinite-rich intervals to
449 eccentricity minima. Charcoal abundance is highest during the seasonal climate of the eccentricity
450 maxima for the SPB (Fig. 2 and 3), in agreement with the previous findings for the LPE (Hollaar et
451 al., 2021, 2023).

452 Both the LPE and SPB study intervals span two 405-kyr cycles (Ruhl et al., 2016; Hinnov et al., 2018;
453 Storm et al., 2020; Pieńkowski et al., 2021). The relative abundance of smectite and the abundance of
454 charcoal both reach a peak during the maxima in the long eccentricity cycle, supporting the notion
455 that orbitally driven changes in seasonal contrast led to high fire activity. Within these long-term
456 trends, the macrocharcoal record also shows ~5 m scale individual peaks or clusters in both the LPE
457 and SPB records (SI Fig. 2, Fig. 2 and 3). Based on the existing age model (Ruhl et al., 2016; Hinnov
458 et al., 2018; Storm et al., 2020; Pieńkowski et al., 2021) we derive that this is the expression of the
459 ~100 kyr eccentricity cycle in the macrocharcoal record. The bandpass filter representing the ~100 kyr
460 cycle in the Pliensbachian of the Mochras core (derived from the Ca and macrocharcoal records),
461 captures the observed ~5 m oscillations in the fire record (SI Fig. 2, Fig. 2 and 3) (Ruhl et al., 2016;
462 Hinnov et al., 2018; Storm et al., 2020; Pieńkowski et al., 2021).

Deleted: 3

Deleted: orbital filter

Deleted: 3

Formatted: Dutch

463 The Sinemurian–Pliensbachian transition is generally associated with an overall warm and humid
464 climate (Korte & Hesselbo, 2011; Gómez et al., 2016), and enhanced levels of runoff and weathering
465 (Bougeault et al., 2017). The results presented here suggest that within this overall warm and humid
466 background, orbital forcing created year-round wet periods, that were not conducive to frequent fire,
467 alternating with periods that remained warm but had a more seasonal climate, that allowed ignition
468 during the dry season. In contrast, the LPE, and the sediments of late Margaritatus ammonite
469 chronozone formed in an overall semi-arid climate with proposed lower runoff levels from the land
470 into the sea (Deconinck et al., 2019; Hollaar et al., 2021; 2023). During the run-up of the LPE we
471 infer orbitally forced alternating climatic states of more extreme seasonality (high fire and smectite)
472 and a more equitable year-round wet climate (low fire and high kaolinite) (Hollaar et al., 2021; 2023)

477 acting within this overall semi-arid climate phase. Overall, kaolinite fluctuates in abundance in
478 opposition to smectite, reflecting hydrological changes from wet and hot to semi-arid and hot, in
479 agreement with high fire activity during a seasonal climate and fire suppression during a year-round
480 wet climate for both the LPE and the SPB.

481 *Vegetation, fire and the intermediate fire-productivity gradient*

482 Fuel (vegetation biomass) and moisture status of the fuel, as governed by seasonal patterns in
483 precipitation and temperature, are the core factors that influence fire behaviour and fire regime
484 (Archibald et al., 2009; Cochrane & Ryan, 2009; Bradstock, 2010; Archibald et al., 2013; Bowman et
485 al., 2014; Archibald et al., 2018). Ecosystems with limited wildfire activity are generally associated
486 with either high precipitation and abundant primary productivity, or low productivity under strongly
487 arid conditions (Pausas & Paula, 2012). In contrast, high wildfire activity occurs in climates that are in
488 the middle of the productivity gradient, where during moist periods plant growth is rapid and biomass
489 builds up forming a connected fuel structure. When followed by periods of drought the fuel moisture
490 content is lowered enabling fire ignition and spread (Pausas & Paula, 2012). Additionally, higher
491 sensitivity to fuel moisture levels in the tropical or mesic areas have been noted, where a small fall in
492 fuel moisture content can lead to more flammable conditions (Cochrane, 2003). Such that the mid
493 points in the intermediate fire-productivity gradient are further enhanced. The intermediate fire-
494 productivity hypothesis (Pausas & Bradstock, 2007; Pausas & Ribeiro, 2013) conceptualizes this
495 relationship between climate-vegetation-fire, where fire activity is plotted along an aridity and
496 productivity gradient (Fig. 5). The observed alternating modes of high and low fire activity, as
497 inferred from the lower Jurassic fossil charcoal record, during the onset of the SPB and LPE, likely
498 indicates shifts in seasonality of the Cardigan Bay Basin hinterland and would place both the LPE and
499 the SPB at intermediate productivity levels during maximum eccentricity forcing. The deep time
500 combined fire and hydrological records we present here are in agreement with the intermediate
501 productivity hypothesis of Pausas & Bradstock (2007) and indicate that even the very different plant
502 functional types and different vegetation assemblages, e.g., a world without grasses, were still subject
503 to this overall fire-productivity gradient control. We indicated on Fig. 5 how these ecosystems without
504 grasses and other flowering plants may have looked in respect to typical Jurassic fuel types. We
505 suggest that both the LPE and the SPB switched between a state of low fire (either limited by climatic
506 aridity or the presence and presence and connectivity of fuel) and a state of high fire during which
507 seasonal contrast is high and an ideal 'fire window' exists in which biomass built up during the wet
508 season after which a fire-prone season followed (Fig. 5).

Deleted: major

Deleted: ing

Deleted: regime and fire behaviour

Deleted: low

Deleted: , where

Deleted: enough

Deleted: to form

Deleted: ,

Deleted: and a

Deleted: allows

Deleted: to lose moisture

Deleted: , which allows

Deleted: more rapid

Deleted: The intermediate fire-productivity hypothesis (Pausas & Bradstock, 2007; Pausas & Ribeiro, 2013) conceptualizes this relationship between climate-vegetation-fire, where fire activity is plotted along an aridity and productivity gradient. On the one extreme, in warm and wet climates fuel is abundant and the fuel structure has a high degree of connectivity, but the high fuel moisture levels limit fire activity (Fig. 5). In contrast, in an arid region, fuel would be sparse and fuel connectivity would be poor limiting fire activity. Although the fuel moisture levels are low and make the fuel that is present flammable, fire is unable to easily spread. Additionally, there is a higher sensitivity to fuel moisture levels in the tropical or mesic areas, where a small fall in fuel moisture content can lead to more flammable conditions (Cochrane, 2003).

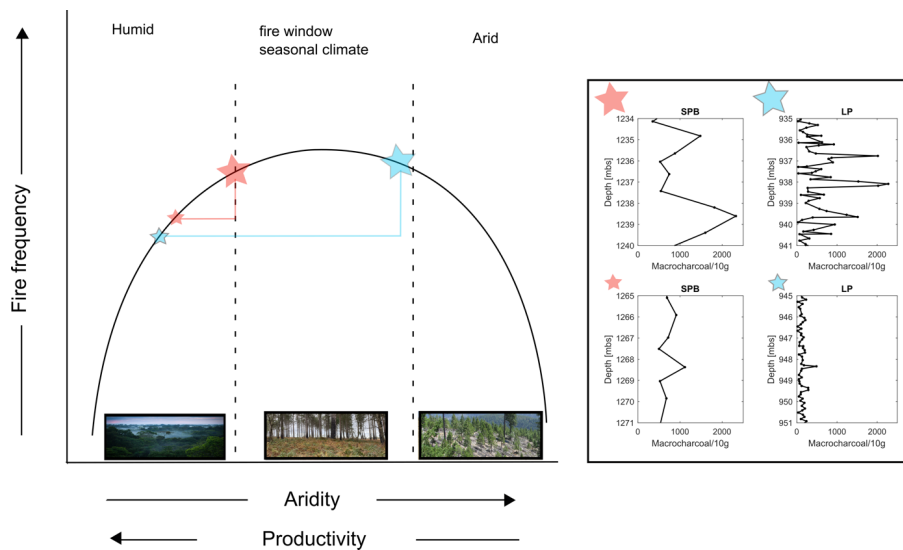
Deleted: ,

Deleted: with

Deleted: vegetation

Deleted: assemblages

Deleted: .



542

543 **Fig. 5: The LPE and SPB fire records placed on the intermediate productivity gradient.** The graph
 544 is adapted from Pausas & Bradstock (2007). Fire frequency is highest in the middle of the hyperbola,
 545 medium levels of aridity and productivity created a seasonal climate in which seasonal biomass
 546 growth was possible (productivity) and seasonally the fuel moisture limits were lower in a season of
 547 drought (aridity), this created the optimized 'fire window'. The SPB is plotted on this fire-productivity
 548 gradient in red: the small star indicates the eccentricity minimum state and the large star the
 549 eccentricity maximum state. The LPE is plotted on the fire-productivity gradient in blue, and again the
 550 small star indicates the eccentricity minimum and the large star the eccentricity maximum. The LPE
 551 has a larger range compared to the SPB, and experienced more fire suppression due to high humidity
 552 levels during eccentricity minima, and also was closer to a productivity limitation state during the
 553 eccentricity maximum.

554 The studied Early Jurassic time-interval likely had five distinct biomes; a seasonal dry (summerwet or
 555 subtropical) biome in the low latitudes, a desert biome in the subtropics, narrow latitudinal bands of a
 556 winterwet biome at low-mid latitude, and warm temperate and cool temperate biomes at mid- and
 557 high-latitudes, respectively (Rees et al., 2000; Willes and McElwain, 2014). The Cardigan Bay Basin
 558 was likely positioned within the winterwet biome at approximately 35 °N (Torsvik et al., 2017). It
 559 therefore would have sat within the bounds of the fire window of the intermediate fire-productivity
 560 hypothesis (Fig. 5). The winterwet biome in both the Sinemurian and Pliensbachian stages were
 561 dominated by conifers as the canopy tree, with a mid-canopy vegetation of cycads and tree-ferns, and
 562 an understory mixture of seed ferns, horsetails and ferns that likely flourished during wetter periods

Deleted: e

Formatted: Font: (Default) Times New Roman, Font colour: Auto

Formatted: Font: (Default) Times New Roman, Font colour: Auto

Formatted: Font: (Default) Times New Roman, Font colour: Auto

Formatted: Font: (Default) Times New Roman, Font colour: Auto

Formatted: Font: (Default) Times New Roman, Font colour: Auto

Formatted: Font: (Default) Times New Roman, Font colour: Auto

Formatted: Font: (Default) Times New Roman, Font colour: Auto

Formatted: Font: (Default) Times New Roman, Font colour: Auto

Formatted: Font: (Default) Times New Roman, Font colour: Auto

Deleted: c

Formatted: Font: (Default) Times New Roman, Font colour: Auto

Deleted: ←

566 (Rees et al., 2000; Slater et al., 2019; Bos et al., 2023). This is evidenced from sporomorph data from
567 the Mochras borehole that hosts abundant fossil pollen in the Sinemurian and Pliensbachian (>94%)
568 (Van de Schootbrugge et al., 2005). Additionally, nearby locations also show evidence of orbitally
569 paced shifts in vegetation assemblages from sites at St. Audries Bay, UK and in NW Germany (Bonis
570 et al., 2010; Bos et al., 2023).

571 During the 100 kyr eccentricity maxima in the UK pollen from the dry-adapted cheirolepidacean
572 conifers is found to be highly abundant (Bonis et al., 2010). Whilst, in Germany a mire-conifer
573 community is apparent with sporomorphs indicating variations in abundance of ferns and fern allies
574 occurring over a 405-kyr eccentricity cycle, with ferns most abundant during eccentricity maxima
575 (Bos et al., 2023).

576 Dry-adapted vegetation, such as the cheirolepidacean conifers likely thrived during more extreme
577 seasonal droughts, maintaining their biomass. In contrast, ferns and fern allies, and mire-conifers as
578 humid-loving plants would grow rapidly during sustained, year-round, periods of rainfall (eccentricity
579 minima), likely inhabiting both open environments and colonising the understory of conifer forests.
580 Furthermore, they would also be able to build dense connected fuel loads during the wet-season of
581 eccentricity maxima, that were then easily dried during the annual dry-season. Ferns, when cured,
582 carry high intensity fires (Adie et al., 2011; Belcher and Hudspith, 2016) and during the Mesozoic
583 'fern prairies' have been linked to intensive surface fires (Harris, 1981; Van Konijnenburg-Van Cittert,
584 2002; Collinson et al., 2007, 2009). Hence, they are suggested to have functioned in a similar fashion
585 to support fires as grasslands and fern stands do today; Mesozoic fern prairies and savannahs therefore
586 likely filled a similar ecological niche to grasses in the modern day (Belcher, 2013 and references
587 therein). Ferns are indeed a common feature of Mesozoic charcoal assemblages, showing their
588 association with fire throughout time (e.g. Collinson et al., 2000; Brown et al., 2012).

589 In the present-day, temperature is an important regulator of fire occurrence. Whilst dead fuel moisture
590 (e.g. that of litter and cured herbaceous components) is primarily influenced by the variability in
591 relative humidity, live fuels are controlled by the combination of temperature and moisture
592 availability, where long periods of drought or heat wave extremes can strongly influence the
593 flammability of live fuels. Sea surface temperatures (TEX⁸⁶) during the Sinemurian and Pliensbachian
594 were at times apparently higher than 28 °C (Robinson et al., 2017). But high-resolution temperature
595 reconstructions are lacking for the Early Jurassic. Orbital forcing of regional–global seawater
596 temperatures occurred throughout the Cenozoic (Westerhold et al., 2020), and likely also the
597 Mesozoic; however, the climate response to changes in orbital insolation is non-linear, and the mean
598 annual insolation is not impacted by precession (Rubicam, 1994). Therefore, the biomes of the SPB
599 not only existed in an overall warm world that was characterized by background orbitally driven

Formatted: Font: (Default) Times New Roman, Font colour: Auto

Formatted: Font: (Default) Times New Roman, Font colour: Auto

Formatted: Font: (Default) Times New Roman, Font colour: Auto

Formatted: Font: (Default) Times New Roman, Font colour: Auto

Formatted: Font: (Default) Times New Roman, Font colour: Auto

Deleted: ¶

Formatted: Font: (Default) Times New Roman, Font colour: Auto

Formatted: Font: (Default) Times New Roman, Font colour: Auto

Formatted: Font: (Default) Times New Roman, Font colour: Auto

Formatted: Font: (Default) Times New Roman, Font colour: Auto

Formatted: Font: (Default) Times New Roman, Font colour: Auto

Formatted: Font: (Default) Times New Roman, Font colour: Auto

Formatted: Font: (Default) Times New Roman, Font colour: Auto

Deleted: ¶

Deleted: ¶

Deleted: ¶

Deleted: ¶

Deleted: (

606 climate shifts across the moister side of the fire-productivity gradient, but superimposed on this live
607 fuels were also responsive to extreme weather linked to periods of drought and heat.

608

609 We propose that the overall humid climate of the SPB fits the high productivity scenario, in which the
610 frequency of flammable conditions is the main factor controlling fire occurrences. No evidence was
611 found to place the SPB on the productivity-limiting high-aridity side of the fire-productivity gradient,
612 where fire frequency would have been mainly influenced by enhanced rainfall in an otherwise dry
613 climate. These findings are in line with the presence of plant cuticle through the studied record,
614 indicating the presence of vegetation throughout this time period and during both phases of high and
615 low modes of fire activity. Hence, the SPB seems to conform to the humid and high productivity end
616 of the aridity gradient (Fig. 5 red lines). Within these constraints (Fig. 5) the SPB is characterized by
617 likely two states across the fire productivity gradient. The biome was situated at the wetter, low fire
618 side of the fire-productivity gradient during eccentricity minima (Fig. 5), and at the seasonal, high fire
619 end of the fire-productivity gradient during eccentricity maxima (but only for each precession half-
620 cycle) (Fig. 5).

621 The fluctuations detected in the present study for the SPB occurred over both long-eccentricity and
622 short eccentricity timescales in the macrocharcoal record, showing longer phases of overall
623 enhancement of fire (405 kyr eccentricity) and relatively abrupt shifts from low to high fire and back
624 again (~100 kyr eccentricity). For this reason, the SPB is placed on a steep portion of the fire-
625 productivity gradient curve (Fig. 5). Overall, the mean charcoal abundance is relatively high, and no
626 sustained periods of very low charcoal abundance are observed in the SPB record, which indicates
627 that the climate never became too wet to fully limit fire activity at that time.

628 The Late Pliensbachian has been linked to a global cooling event, with a potential of 5–7 °C lowering
629 in temperature inferred for the NW Tethys region (Korte et al., 2015). The atmospheric moisture
630 holding capacity of a cooler climate is lower compared to a warm climate, in which a 1 °C cooling
631 likely lowers the water holding capacity of air by 7% (Trenberth et al., 2005). The presence of
632 terrestrial phytoclasts throughout confirms the presence of vegetation in the surrounding landmasses
633 throughout this period. The mean abundance of charcoal for the LPE section is slightly lower than that
634 of the SPB and the lowest charcoal abundances are coeval with a K/I enhancement, suggesting that
635 during eccentricity minima environmental conditions moved further into the humid zone of the fire-
636 productivity gradient (Fig. 5 blue line). Increasing eccentricity shifted the system to a more seasonal
637 climate where the fire and clay records indicate the presence of a wet season that allowed for build-up
638 of biomass followed by a dry season in which fire was able to be ignited and spread.

639 Conceptually, the relatively drier and cooler LPE climate would have resulted in conditions that are
640 more arid, shifting to the biomass-limited part of the productivity/aridity – fire frequency gradient

Deleted: ¶

Deleted: Hence, in the more highly productive ecosystems fire activity is forced by the frequency of dry weather/flamable conditions (Pausas & Paula, 2012). Low fire activity in the Lower Jurassic section studied here is found to occur at times of high kaolinite/illite ratios, which indicates an enhanced hydrological cycle, and likely a year-round wet climate. ¶

Deleted: Vegetation growth likely occurred year-round in this warm and wet climate.

Deleted:

Deleted: spectrum

Deleted: that would have enabled biomass growth and fuel connectivity

Deleted: interval

Deleted:

Deleted: modes of

Deleted: exists two

Deleted: for the SPB; the wetter end of the spectrum occurred

Deleted: on

Deleted: conditions enter the seasonal side of the fire-productivity gradient (towards aridity) to allow an increase in fire activity. ...wreat times apparently , although h-. F,whilst¶

Deleted: wreat times apparently , although h-. F,whilst¶

Deleted: long

Deleted: -

668 during eccentricity maxima, compared to the SPB (Fig. 5 blue lines). This is supported by the large
669 fluctuations observed between low fire frequency and high fire frequency for the LPE and the fact that
670 estimated high fire periods did not occur suddenly, but rather were sustained over a larger part of the
671 cycle. Therefore, the phase of highest fire frequency operating in the seasonal ‘fire window’ as
672 indicated in figure 5 for the LPE (blue lines) likely occurred for a larger part of the fire productivity
673 gradient. Hence, conditions across the LPE occurred across a wider range of the productivity/aridity
674 **spectrum of the fire frequency gradient** (Fig. 5 blue lines) compared to the SPB. There is no evidence
675 that conditions ever became limited by aridity, and conditions during the LPE did not extend beyond
676 the seasonal fire window into the arid part of the productivity/aridity **spectrum** of the fire frequency
677 gradient.

678 Importantly, the Jurassic climate was overall warm and humid, about 5–10 °C warmer on global
679 average compared to today (e.g., Rees et al., 2000; Sellwood & Valdes, 2008), with ~ 3.5–10 times the
680 pre-industrial value of atmospheric $p\text{CO}_2$ during the Early Jurassic (e.g. Retallack, 2001; Beerling &
681 Royer, 2002; McElwain et al., 2005; Berner, 2006; Steinthorsdottir & Vajda, 2015; Li et al., 2020). In
682 this context, it may not be surprising that a relative cooling event in the Early Jurassic did not lead to
683 the aridity and biomass-limiting conditions observed during the last glacial period, at latitudes of ~38
684 °C N (Daniau et al., 2007).

685 5 Conclusions

686 The study of two different climatic ‘background’ states, at the LPE and the SPB, shows that fire
687 activity was strongly modulated by orbital eccentricity cycles. The 405 kyr shifts in the record of
688 wildfire prevalence reflect similar changes also in the hydrological cycle (based on clay mineralogy
689 data) showing that high fire activity occurred during periods of high seasonal contrast and that fire
690 activity was suppressed during periods of high year-round humidity, because the latter would have
691 enhanced the fuel moisture levels and prevented frequent ignition and sustained fire spread. The fire
692 record of both climatic events is limited by the high fuel moisture levels during eccentricity minima,
693 but fires were more prevalent during times of increased seasonality, every precession half-cycle
694 during eccentricity maxima. Hence, during both events fire activity was limited by fuel moisture
695 content and not by productivity. Both the SPB and the LPE climate systems were therefore situated on
696 the moisture-limited side of the intermediate fire-productivity gradient (Fig. 5). Due to the lower
697 moisture-holding capacity of cold air, the overall higher seasonality of the Late Pliensbachian and the
698 more sustained high fire-frequency periods (based on the charcoal record for the LPE) we place the
699 LPE towards the higher end of the aridity gradient, within maximum seasonality and maximum fire
700 frequency window of the fire productivity graph (Fig. 5). The SPB fire regime reflected a more humid
701 climate that shifted abruptly between low fire frequency to high fire frequency within less extreme
702 bounds on the aridity gradient. This research reveals that the intermediate-fire productivity hypothesis
703 (Pausas & Bradstock, 2007) can also be applied to high-resolution deep time records, before the

Deleted: the

Deleted: the

Deleted: gradient

707 [evolution of grasses](#) and that this hypothesis explains well the influence of orbital cycles within
708 different overall climate states, be they cooling or warming trends. The coupling of high-resolution
709 clay mineralogy and fossil charcoal records, combined with constraints on orbital forcing at such
710 time, allows for inferences on how Earth's natural climate state variability has driven shifts in
711 terrestrial productivity through the geological past.

712 **Acknowledgements**

713 This is a contribution to the JET project funded by the Natural Environment Research Council
714 (NERC) (grant number NE/N018508/1). All authors acknowledge funding from the International
715 Continental Scientific Drilling Program (ICDP) and TPH acknowledges funding from the University
716 of Exeter.

717 **Conflict of Interest**

718 The authors declare no conflicts of interest relevant to this study.

719 **Data Availability Statement**

720 Supplementary data are available at the National Geoscience Data Centre at Keyworth (NGDC)
721 at <https://doi.org/10.5285/1461dbe5-50a8-425c-8c49-ac1f04bcc271> (Hollaar, 2022) for the interval
722 934–918 m. b.s. All data presented for the interval 951–934 m. b.s. are available at the National
723 Geoscience Data Centre at Keyworth (NGDC) at [https://doi.org/10.5285/d6b7c567-49f0-44c7-a94c-
724 e82fa17ff98e](https://doi.org/10.5285/d6b7c567-49f0-44c7-a94c-e82fa17ff98e) (Hollaar et al., 2021b). All data for the interval 1271–1233 mbs is deposited at the
725 University of Exeter: <http://hdl.handle.net/10871/133255>.

726 **Supporting Information**

727

728 **References**

- 729 [Adie, H., Richert, S., Kirkman, K. P., & Lawes, M. J. \(2011\). The heat is on: frequent high intensity
730 fire in bracken \(*Pteridium aquilinum*\) drives mortality of the sprouting tree *Protea caffra* in temperate
731 grasslands. *Plant Ecology*, 212, 2013 – 2022. <https://doi.org/10.1007/s11258-011-9945-8>](#)
- 732 Archibald, S., Lehmann, C. E., Belcher, C. M., Bond, W. J., Bradstock, R. A., Daniau, A. L., et al.
733 (2018). Biological and geophysical feedbacks with fire in the Earth system. *Environmental Research
734 Letters*, 13(3), 033003. <https://doi.org/10.1088/1748-9326/aa9ead>
- 735 Archibald, S., Lehmann, C. E., Gómez-Dans, J. L., & Bradstock, R. A. (2013). Defining pyromes and
736 global syndromes of fire regimes. *Proceedings of the National Academy of Sciences*, 110(16), 6442 –
737 6447. <https://doi.org/10.1073/pnas.1211466110>

738 Archibald, S., Roy, D. P., van Wilgen, B. W., & Scholes, R. J. (2009). What limits fire? An
739 examination of drivers of burnt area in Southern Africa. *Global Change Biology*, 15(3), 613 – 630.
740 <https://doi.org/10.1111/j.1365-2486.2008.01754.x>

741 Beerling, D. J., & Royer, D. L. (2002). Fossil plants as indicators of the Phanerozoic global carbon
742 cycle. *Annual Review of Earth and Planetary Sciences*, 30(1), 527 – 556.
743 <https://doi.org/10.1146/annurev.earth.30.091201.141413>

744 Belcher, C. M., Collinson, M. E., & Scott, A. C. (2005). Constraints on the thermal energy released
745 from the Chicxulub impactor: new evidence from multi-method charcoal analysis. *Journal of the*
746 *Geological Society*, 162(4), 591 – 602. <https://doi.org/10.1144/0016-764904-104>

747 [Belcher, C. M., Collinson, M. E., & Scott, A. C. \(2013\). A 450-Million-Year History of Fire. In C. M.](#)
748 [Belcher \(Eds.\). *Fire Phenomena and the Earth System*, \(pp. 240 – 241\). London, UK: Wiley.](#)

749 [Belcher, C. M., & Hudspith, V. A. \(2017\). Changes to Cretaceous surface fire behaviour influenced](#)
750 [the spread of the early angiosperms. *New Phytologist*, 213\(3\), 1521 – 1532.](#)
751 <https://doi.org/10.1111/nph.14264>

752 Berger, A., Loutre, M. F. & Dehant, V. Astronomical frequencies for pre-Quaternary palaeoclimate
753 studies. *Terra Nova* 1, 474–479 (1989). <https://doi.org/10.1111/j.1365-3121.1989.tb00413.x>

754 Berner, R. A. (2006). GEOCARBSULF: a combined model for Phanerozoic atmospheric O₂ and
755 CO₂. *Geochimica et Cosmochimica Acta*, 70(23), 5653 – 5664.
756 <https://doi.org/10.1016/j.gca.2005.11.032>

757 [Bonis, N. R., Ruhl, M., & Kürschner, W. M. \(2010\). Milankovitch-scale palynological turnover across](#)
758 [the Triassic–Jurassic transition at St. Audrie's Bay, SW UK. *Journal of the Geological Society*, 167\(5\),](#)
759 [877–888. <https://doi.org/10.1144/0016-76492009-141>](#)

760 [Bos, R., Lindström, S., van Konijnenburg-van Cittert, H., Hilgen, F., Hollaar, T. P., Aalpoel, H., et al.](#)
761 [\(2023\). Triassic-Jurassic vegetation response to carbon cycle perturbations and climate](#)
762 [change. *Global and Planetary Change*, 228, 104211. <https://doi.org/10.1016/j.gloplacha.2023.104211>](#)

763 Bougeault, C., Pellenard, P., Deconinck, J. F., Hesselbo, S. P., Dommergues, J. L., Bruneau, L., et al.
764 (2017). Climatic and palaeoceanographic changes during the Pliensbachian (Early Jurassic) inferred
765 from clay mineralogy and stable isotope (CO) geochemistry (NW Europe). *Global and Planetary*
766 *Change*, 149, 139 – 152. <https://doi.org/10.1016/j.gloplacha.2017.01.005>

767 Bowman, D. M., Murphy, B. P., Williamson, G. J., & Cochrane, M. A. (2014). Pyrogeographic
768 models, feedbacks and the future of global fire regimes. *Global Ecology and Biogeography*, 23(7),
769 821 – 824. <https://doi.org/10.1111/geb.12180>

Formatted: Font: (Default) Times New Roman, 11 pt

Formatted: Font: (Default) Times New Roman, 11 pt, Not Italic

Formatted: Font: (Default) Times New Roman, 11 pt

Formatted: Ligatures: Standard + Contextual

Formatted: English (US)

Formatted: Font: (Default) Times New Roman, 11 pt, Not Bold, Ligatures: None

Formatted: Ligatures: Standard + Contextual

Field Code Changed

Formatted: Underline, Font colour: Hyperlink, Ligatures: None

Formatted: Font: (Default) Times New Roman, Underline, Font colour: Hyperlink, Ligatures: None

Formatted: Underline, Font colour: Hyperlink

Formatted: Font: (Default) Times New Roman, Underline, Font colour: Hyperlink, Ligatures: None

Formatted: Underline, Font colour: Hyperlink, Ligatures: None

Formatted: Font: (Default) Times New Roman, Underline, Font colour: Hyperlink, Ligatures: None

Formatted: English (UK)

Formatted: Font: (Default) Times New Roman, Underline, Font colour: Hyperlink, Ligatures: None

Formatted: Font: (Default) Times New Roman

770 Bradstock, R. A. (2010). A biogeographic model of fire regimes in Australia: current and future
771 implications. *Global Ecology and Biogeography*, 19(2), 145 – 158. <https://doi.org/10.1111/j.1466-8238.2009.00512.x>

773 [Brown, S. A., Scott, A. C., Glasspool, I. J., & Collinson, M. E. \(2012\). Cretaceous wildfires and their impact on the Earth system. *Cretaceous research*, 36, 162 – 190. <https://doi.org/10.1016/j.cretres.2012.02.008>](#)

776 Chamley, H. (1989). *Clay Sedimentology*. Heidelberg: Springer Berlin Heidelberg.

777 Cochrane, M. A. (2003). Fire science for rainforests. *Nature*, 421(6926), 913 – 919.
778 <https://doi.org/10.1038/nature01437>

779 Cochrane, M. A., & Ryan, K. C. (2009). Fire and fire ecology: Concepts and principles. *Tropical fire ecology*, 25 – 62. https://doi.org/10.1007/978-3-540-77381-8_2

781 [Collinson, M.E., Featherstone, C., Cripps, J.A., Nichols, G.J., & Scott, A.C. \(2000\). Charcoal-rich plant debris accumulations in the Lower Cretaceous of the Isle of Wight, England. *Acta Palaeobotanica, Supplement 2*, 93 – 105.](#)

784 [Collinson, M. E., Steart, D. C., Harrington, G. J., Hooker, J. J., Scob, A. C., Allen, L. O. et al. \(2009\). Palynological evidence of vegetation dynamics in response to palaeoenvironmental change across the onset of the Paleocene-Eocene Thermal Maximum at Cobham, Southern England. *Grana*, 48\(1\), 38 – 66. <https://doi.org/10.1080/00173130802707980>](#)

788 [Collinson, M. E., Steart, D. C., Scob, A. C., Glasspool, I. J., & Hooker, J. J. \(2007\). Episodic fire, runoff and deposition at the Palaeocene–Eocene boundary. *Journal of the Geological Society*, 164\(1\), 87 – 97. <https://doi.org/10.1144/0016-76492005-185>](#)

791 Daniau, A. L., Bartlein, P. J., Harrison, S. P., Prentice, I. C., Brewer, S., Friedlingstein, P., et al.
792 (2012). Predictability of biomass burning in response to climate changes. *Global Biogeochemical Cycles*, 26(4). <https://doi.org/10.1029/2011GB004249>

794 Daniau, A. L., Sánchez-Goñi, M. F., Beaufort, L., Laggoun-Défarge, F., Loutre, M. F., & Duprat, J.
795 (2007). Dansgaard–Oeschger climatic variability revealed by fire emissions in southwestern Iberia. *Quaternary Science Reviews*, 26(9-10), 1369 – 1383.
796 <https://doi.org/10.1016/j.quascirev.2007.02.005>

798 Danisch, J., Kabiri, L., Nutz, A., & Bodin, S. (2019). Chemostratigraphy of late Sinemurian–early Pliensbachian shallow-to deep-water deposits of the Central High Atlas Basin: Paleoenvironmental

Formatted: Font: (Default) Times New Roman, 11 pt, Font colour: Auto, Pattern: Clear, Ligatures: None

Formatted: Font: (Default) Times New Roman, 11 pt, Font colour: Auto, Pattern: Clear, Ligatures: None

Formatted: Font: (Default) Times New Roman, Underline, Font colour: Hyperlink, Ligatures: None

Formatted: Font: Not Italic

Formatted: English (US)

Formatted: English (US)

Formatted: English (US)

Formatted: English (US)

Formatted: English (US)

Formatted: English (US)

Formatted: Space Before: Auto

Formatted: English (US)

Formatted: Font: Italic

Formatted: Dutch

Formatted: dx-doi

Formatted: Font: (Default) Times New Roman, 11 pt, Underline, Font colour: Hyperlink, English (UK)

Formatted: Font: (Default) Open Sans, 10 pt, Font colour: Dark Grey

Formatted: Don't adjust space between Latin and Asian text, Don't adjust space between Asian text and numbers

Formatted: Font: (Default) Times New Roman, Underline, Font colour: Hyperlink, Ligatures: None

Formatted: Font colour: Text 1, Ligatures: Standard + Contextual

800 implications. *Journal of African Earth Sciences*, 153, 239 – 249.
801 <https://doi.org/10.1016/j.jafrearsci.2019.03.003>

802 Deconinck, J. F., Hesselbo, S. P., & Pellenard, P. (2019). Climatic and sea-level control of Jurassic
803 (Pliensbachian) clay mineral sedimentation in the Cardigan Bay Basin, Llanbedr (Mochras Farm)
804 borehole, Wales. *Sedimentology*, 66(7), 2769 – 2783. <https://doi.org/10.1111/sed.12610>

805 De Graciansky, P. C., Dardeau, G., Dommergues, J. L., Durllet, C., Marchand, D., Dumont, T., et al.
806 (1998). Ammonite biostratigraphic correlation and Early Jurassic sequence stratigraphy in France:
807 comparisons with some UK sections. In: de Graciansky, P.C., Hardenbol, J., Jacquin, T., Farley, M. &
808 Vail, P.R. (Eds.), *Mesozoic and Cenozoic Sequence Stratigraphy of European Basins. Special*
809 *Publication of the Society for Sedimentary Geology (SEPM)*, 60, 583 – 622.

810 Glasspool, I. J., Edwards, D., & Axe, L. (2004). Charcoal in the Silurian as evidence for the earliest
811 wildfire. *Geology*, 32(5), 381 – 383. <https://doi.org/10.1130/G20363.1>

812 Glasspool, I. J., & Gastaldo, R. A. (2022). Silurian wildfire proxies and atmospheric oxygen.
813 *Geology*. <https://doi.org/10.1130/G50193.1>

814 Gómez, J. J., Comas-Rengifo, M. J., & Goy, A. (2016). Palaeoclimatic oscillations in the
815 Pliensbachian (Early Jurassic) of the Asturian Basin (Northern Spain). *Climate of the Past*, 12(5),
816 1199 – 1214. <https://doi.org/10.5194/cp-12-1199-2016>

817 *Harris, T. M. (1981). Burnt ferns from the English Wealden. Proceedings of the Geologists'*
818 *Association*, 92(1), 47 – 58. [https://doi.org/10.1016/S0016-7878\(81\)80019-3](https://doi.org/10.1016/S0016-7878(81)80019-3)

819 Haq, B. U. (2018). Jurassic sea-level variations: a reappraisal. *GSA today*, 28(1), 4 – 10.
820 <https://doi.org/10.1130/GSATG359A.1>

821 Hinnov, L. A., Ruhl, M. R., & Hesselbo, S. P. (2018). Reply to the Comment on “Astronomical
822 constraints on the duration of the Early Jurassic Pliensbachian Stage and global climatic fluctuations”
823 (Ruhl *et al.*, (2016). *Earth and Planetary Science Letters*, 455, 149 – 165).
824 <https://doi.org/10.1016/j.epsl.2017.10.061>

825 Hesselbo, S.P. & Jenkyns, H.C. (1998). British Lower Jurassic sequence stratigraphy. In: de
826 Graciansky, P.C., Hardenbol, J., Jacquin, T., Farley, M. & Vail, P.R. (Eds.), *Mesozoic–Cenozoic*
827 *Sequence Stratigraphy of European Basins. Special Publication of the Society for Sedimentary*
828 *Geology (SEPM)*, 60, 561 – 581.

829 Hollaar, T. P., Baker, S. J., Hesselbo, S. P., Deconinck, J. F., Mander, L., Ruhl, M., & Belcher, C. M.
830 (2021). Wildfire activity enhanced during phases of maximum orbital eccentricity and precessional

Formatted: Don't adjust space between Latin and Asian text, Don't adjust space between Asian text and numbers

Formatted: Font: (Default) Times New Roman, Underline, Font colour: Hyperlink, Ligatures: None

Formatted: Font: Italic, Font colour: Text 1, Ligatures: Standard + Contextual

831 forcing in the Early Jurassic. *Communications Earth & Environment*, 2(1), 1 – 12.
832 <https://doi.org/10.1038/s43247-021-00307-3>

833 Hollaar, T. P., Hesselbo, S. P., Deconinck, J. F., Damaschke, M., Ullmann, C. V., Jiang, M., &
834 Belcher, C. M. (2023). Environmental changes during the onset of the Late Pliensbachian Event
835 (Early Jurassic) in the Cardigan Bay Basin, Wales. *Climate of the Past*, 19(5), 979-997.
836 <https://doi.org/10.5194/cp-19-979-2023>

837 Imbrie, J., & Imbrie, J. Z. (1980). Modeling the climatic response to orbital variations. *Science*,
838 207(4434), 943 – 953. <https://doi.org/10.1126/science.207.4434.943>

839 Korte, C. & Hesselbo, S. P. (2011). Shallow marine carbon and oxygen isotope and elemental records
840 indicate icehouse-greenhouse cycles during the Early Jurassic. *Paleoceanography*, 26(4).
841 <https://doi.org/10.1029/2011PA002160>

842 Korte, C., Hesselbo, S. P., Ullmann, C. V., Dietl, G., Ruhl, M., Schweigert, G., & Thibault, N. (2015).
843 Jurassic climate mode governed by ocean gateway. *Nature communications*, 6(1), 1 – 7.
844 <https://doi.org/10.1038/ncomms10015>

845 Krawchuk, M. A., & Moritz, M. A. (2011). Constraints on global fire activity vary across a resource
846 gradient. *Ecology*, 92(1), 121 – 132. <https://doi.org/10.1890/09-1843.1>

847 Legarreta, L., & Uliana, M. A. (1996). The Jurassic succession in west-central Argentina: stratal
848 patterns, sequences and paleogeographic evolution. *Palaeogeography, Palaeoclimatology,*
849 *Palaeoecology*, 120(3-4), 303 – 330. [https://doi.org/10.1016/0031-0182\(95\)00042-9](https://doi.org/10.1016/0031-0182(95)00042-9)

850 Li, X., Wang, J., Rasbury, T., Zhou, M., Wei, Z., & Zhang, C. (2020). Early Jurassic climate and
851 atmospheric CO₂ concentration in the Sichuan paleobasin, southwestern China. *Climate of the Past*,
852 16(6), 2055 – 2074. <https://doi.org/10.5194/cp-16-2055-2020>

853 Martinez, M. & Dera, G. (2015). Orbital pacing of carbon fluxes by a ~9-My eccentricity cycle
854 during the Mesozoic. *Proceedings of the National Academy of Sciences*, 112, 12604 – 12609.
855 <https://doi.org/10.1073/pnas.141994611>

856 McElwain, J. C., Wade-Murphy, J., & Hesselbo, S. P. (2005). Changes in carbon dioxide during an
857 oceanic anoxic event linked to intrusion into Gondwana coals. *Nature*, 435(7041), 479 – 482.
858 <https://doi.org/10.1038/nature03618>

859 Meyn, A., White, P. S., Buhk, C., & Jentsch, A. (2007). Environmental drivers of large, infrequent
860 wildfires: the emerging conceptual model. *Progress in Physical Geography*, 31(3), 287 – 312.
861 <https://doi.org/10.1177/0309133307079365>

Formatted: Dutch

Field Code Changed

- 862 Moore, D. M. & Reynolds Jr, R. C. (1997). *X-ray Diffraction and the Identification and Analysis of*
863 *Clay Minerals*. Oxford: Oxford University Press.
- 864 Munier, T., Deconinck, J. F., Pellenard, P., Hesselbo, S. P., Riding, J. B., Ullmann, C. V., et al.
865 (2021). Million-year-scale alternation of warm–humid and semi-arid periods as a mid-latitude climate
866 mode in the Early Jurassic (late Sinemurian, Laurusian Seaway). *Climate of the Past*, 17(4), 1547 –
867 1566. <https://doi.org/10.5194/cp-17-1547-2021>
- 868 Oboh-Ikuenobe, F. E., Obi, C. G. & Jaramillo, C. A. (2005). Lithofacies, palynofacies, and sequence
869 stratigraphy of Palaeogene strata in Southeastern Nigeria. *Journal of African Earth Sciences*, 41, 79–
870 101. <https://doi.org/10.1016/j.jafrearsci.2005.02.002>
- 871 Pausas, J. G., & Bradstock, R. A. (2007). Fire persistence traits of plants along a productivity and
872 disturbance gradient in mediterranean shrublands of south-east Australia. *Global Ecology and*
873 *Biogeography*, 16(3), 330 – 340. <https://doi.org/10.1111/j.1466-8238.2006.00283.x>
- 874 Pausas, J. G., & Paula, S. (2012). Fuel shapes the fire–climate relationship: evidence from
875 Mediterranean ecosystems. *Global Ecology and Biogeography*, 21(11), 1074 – 1082.
876 <https://doi.org/10.1111/j.1466-8238.2012.00769.x>
- 877 Pausas, J. G., & Ribeiro, E. (2013). The global fire–productivity relationship. *Global Ecology and*
878 *Biogeography*, 22(6), 728 – 736. <https://doi.org/10.1111/geb.12043>
- 879 Petschick, R. MacDiff 4.1. 2. Powder diffraction software (2000). Available from the author at
880 <http://www.geol.uni-erlangen.de/html/software/Macdiff.html>.
- 881 Pieńkowski, G., Uchman, A., Ninard, K., & Hesselbo, S. P. (2021). Ichnology, sedimentology, and
882 orbital cycles in the hemipelagic Early Jurassic Laurusian Seaway (Pliensbachian, Cardigan Bay
883 Basin, UK). *Global and Planetary Change*, 207, 103648.
884 <https://doi.org/10.1016/j.gloplacha.2021.103648>
- 885 Rees, P. M., Ziegler, A. M. & Valdes, P. J. (2000). Jurassic phytogeography and climates: new data
886 and model comparisons. In Huber, B. T., Macleod, K. G. & Wing, S. L. (Eds.), *Warm Climates in*
887 *Earth History*. (pp. 297 – 318). Cambridge: Cambridge University Press.
- 888 Retallack, G. J. (2001). A 300-million-year record of atmospheric carbon dioxide from fossil plant
889 cuticles. *Nature*, 411(6835), 287 – 290. <https://doi.org/10.1038/35077041>
- 890 Riding, J. B., Leng, M. J., Kender, S., Hesselbo, S. P., & Feist-Burkhardt, S. (2013). Isotopic and
891 palynological evidence for a new Early Jurassic environmental perturbation. *Palaeogeography,*
892 *Palaeoclimatology, Palaeoecology*, 374, 16 – 27. <https://doi.org/10.1016/j.palaeo.2012.10.019>

Field Code Changed

893 [Robinson, S. A., Ruhl, M., Astley, D. L., Naafs, B. D. A., Farnsworth, A. J., Bown, P. R. et al. \(2017\).](#)
894 [Early Jurassic North Atlantic sea-surface temperatures from TEX₈₆ palaeothermometry.](#)
895 [Sedimentology](#), 64(1), 215 – 230. <https://doi.org/10.1111/sed.12321>

896 [Rubincam, D. P. \(1994\). Insolation in terms of Earth's orbital parameters.](#) *Theoretical and applied*
897 *climatology*, 48, 195 – 202. <https://doi.org/10.1007/BF00867049>

898 Ruffell, A., McKinley, J. M. & Worden, R. H. (2002). Comparison of clay mineral stratigraphy to
899 other proxy palaeoclimate indicators in the Mesozoic of NW Europe. *Philosophical Transactions of*
900 *the Royal Society London A: Mathematical, Physical and Engineering Sciences*, 360, 675 – 693.
901 <https://doi.org/10.1098/rsta.2001.0961>

902 Ruhl, M., Hesselbo, S. P., Hinnov, L., Jenkyns, H. C., Xu, W., Riding, J. B., et al. (2016).
903 Astronomical constraints on the duration of the Early Jurassic Pliensbachian Stage and global climatic
904 fluctuations. *Earth and Planetary Science Letters*, 455, 149 – 165.
905 <https://doi.org/10.1016/j.epsl.2016.08.038>

906 [Scott, A. C. \(2000\). The Pre-Quaternary history of fire.](#) *Palaeogeography, Palaeoclimatology,*
907 *Palaeoecology*, 164(1-4), 281 – 329. [https://doi.org/10.1016/S0031-0182\(00\)00192-9](https://doi.org/10.1016/S0031-0182(00)00192-9)

908 [Scott, A. C., & Damblon, F. \(2010\). Charcoal: Taphonomy and significance in geology, botany and](#)
909 [archaeology.](#) *Palaeogeography, Palaeoclimatology, Palaeoecology*, 291(1-2), 1 – 10.
910 <https://doi.org/10.1016/j.palaeo.2010.03.044>

911 Sellwood, B. W., & Valdes, P. J. (2008). Jurassic climates. *Proceedings of the Geologists'*
912 *Association*, 119(1), 5 – 17. [https://doi.org/10.1016/S0016-7878\(59\)80068-7](https://doi.org/10.1016/S0016-7878(59)80068-7)

913 Silva, R. L., Duarte, L. V., Wach, G. D., Ruhl, M., Sadki, D., Gómez, J. J. et al. (2021). An Early
914 Jurassic (Sinemurian–Toarcian) stratigraphic framework for the occurrence of organic matter
915 preservation intervals (OMPIs). *Earth-Science Reviews*, 221, 103780.

916 [Slater, S. M., Twitchett, R. J., Danise, S., & Vajda, V. \(2019\). Substantial vegetation response to Early](#)
917 [Jurassic global warming with impacts on oceanic anoxia.](#) *Nature Geoscience*, 12(6), 462 – 467.
918 <https://doi.org/10.1038/s41561-019-0349-z>

919 Steinthorsdottir, M., & Vajda, V. (2015). Early Jurassic (late Pliensbachian) CO₂ concentrations
920 based on stomatal analysis of fossil conifer leaves from eastern Australia. *Gondwana Research*, 27(3),
921 932 – 939. <https://doi.org/10.1016/j.gr.2013.08.021>

922 Storm, M. S., Hesselbo, S. P., Jenkyns, H. C., Ruhl, M., Ullmann, C. V., Xu, W., et al. (2020). Orbital
923 pacing and secular evolution of the Early Jurassic carbon cycle. *Proceedings of the National Academy*
924 *of Sciences*, 117(8), 3974 – 3982. <https://doi.org/10.1073/pnas.1912094117>

Formatted: Superscript

Formatted: Font: (Default) Times New Roman, Underline, Font colour: Hyperlink, Ligatures: None

Formatted: Font: Italic

Formatted: Underline, Font colour: Hyperlink, Ligatures: None

Formatted: Font: (Default) Times New Roman, Underline, Font colour: Hyperlink, Pattern: Clear, Ligatures: None

Formatted: English (US)

Formatted: Font: (Default) Times New Roman, Underline, Font colour: Hyperlink, Ligatures: None

Formatted: Font: Italic

Formatted: English (US)

Formatted: Font: (Default) Times New Roman, Underline, Font colour: Hyperlink, Ligatures: None

Formatted: English (UK)

Formatted: Font: Italic

Formatted: Font: (Default) Times New Roman, Underline, Font colour: Hyperlink, Pattern: Clear, Ligatures: None

Formatted: Ligatures: Standard + Contextual

925 Torsvik, T. H., & Cocks, L. R. M. (2017). Jurassic. In *Earth History and Palaeogeography*.
 926 Cambridge: Cambridge University Press.

927 Trenberth, K. E., Fasullo, J., & Smith, L. (2005). Trends and variability in column-integrated
 928 atmospheric water vapor. *Climate dynamics*, 24(7), 741 – 758. [https://doi.org/10.1007/s00382-005-](https://doi.org/10.1007/s00382-005-0017-4)
 929 [0017-4](https://doi.org/10.1007/s00382-005-0017-4)

930 Ullmann, C. V., Szűcs, D., Jiang, M., Hudson, A. J., & Hesselbo, S. P. (2022). Geochemistry of
 931 microfossil, bulk rock and secondary calcite in the Early Jurassic strata of the Llanbedr (Mochras
 932 Farm) drill core, Cardigan Bay Basin, Wales, UK. *Journal of the Geological Society*, 179(1).
 933 <https://doi.org/10.1144/jgs2021-018>

934 van de Schootbrugge, B., Bailey, T. R., Rosenthal, Y., Katz, M. E., Wright, J. D., Miller, K. G., et al.
 935 (2005). Early Jurassic climate change and the radiation of organic-walled phytoplankton in the Tethys
 936 Ocean. *Paleobiology*, 31(1), 73 – 97. [https://doi.org/10.1666/0094-](https://doi.org/10.1666/0094-8373(2005)031<0073:EJCCAT>2.0.CO;2)
 937 [8373\(2005\)031<0073:EJCCAT>2.0.CO;2](https://doi.org/10.1666/0094-8373(2005)031<0073:EJCCAT>2.0.CO;2)

938 van der Werf, G. R., Randerson, J. T., Giglio, L., Collatz, G. J., Kasibhatla, P. S., & Arellano Jr, A. F.
 939 (2006). Interannual variability in global biomass burning emissions from 1997 to 2004. *Atmospheric*
 940 *Chemistry and Physics*, 6(11), 3423 – 3441. <https://doi.org/10.5194/acp-6-3423-2006>

941 Van Konijnenburg-Van Cibert, J. H. A. (2002). Ecology of some late Triassic to early Cretaceous
 942 ferns in Eurasia. *Review of Palaeobotany and Palynology*, 119(1-2), 113 – 124.
 943 [https://doi.org/10.1016/S0034-6667\(01\)00132-4](https://doi.org/10.1016/S0034-6667(01)00132-4)

944 Westerhold, T., Marwan, N., Drury, A. J., Liebrand, D., Agnini, C., Anagnostou, E. et al. (2020). An
 945 astronomically dated record of Earth's climate and its predictability over the last 66 million years.
 946 *Science*, 369(6509), 1383 – 1387. <https://doi.org/10.1126/science.aba6853>

947 [Willes, K. & McElwain, J. \(2014\) The Evolution of Plants, Oxford University Press.](#)

Formatted: Dutch

Formatted: Dutch

Formatted: Dutch

Formatted: Dutch

Formatted: Don't adjust space between Latin and Asian text, Don't adjust space between Asian text and numbers

Formatted: Underline, Font colour: Hyperlink, Ligatures: None

Formatted: Font colour: Text 1, Ligatures: Standard + Contextual

Formatted: Underline, Font colour: Hyperlink, Ligatures: None

Formatted: Font: (Default) Times New Roman, Underline, Font colour: Hyperlink, Ligatures: None

Deleted: ¶
¶

Formatted: Font: (Default) Times New Roman, Font colour: Text 1

Formatted: Font colour: Text 1

Formatted: Font: (Default) Times New Roman, Font colour: Text 1

Formatted: Font colour: Text 1

Formatted: Font: (Default) Times New Roman, Font colour: Text 1